SHORT COMMUNICATION

Journal of Semiconductors
(2021) 42, 090501
doi: 10.1088/1674-4926/42/9/090501

Investigating the reason for high FF from ternary organic solar cells

Danqin Li[1, ‡], Yihan Zeng[1, ‡], Zeng Chen[3], Shifeng Leng[4], Zuo Xiao[5], Qifan Xue[6], Tianyu Hao[4], Meng Lv[1], Hongbo Wu[7], Lina Lin[1], Jianming Yang[1], Zaifei Ma[7], Jinquan Chen[1], Rong Huang[1], Feng Liu[4], Haiming Zhu[3], Xianjie Liu[8], Liming Ding[5, †], Mats Fahlman[8], and Qinye Bao[1, 2, 6, †]

[1]School of Physics and Electronic Science, East China Normal University, Shanghai 200241, China

[2]Collaborative Innovation Center of Extreme Optics, Shanxi University, Taiyuan 030006, China

[3]Department of Chemistry, Zhejiang University, Hangzhou 310027, China

[4]School of Chemistry and Chemical Engineering, Shanghai Jiao Tong University, Shanghai 200025, China

[5]Center for Excellence in Nanoscience (CAS), Key Laboratory of Nanosystem and Hierarchical Fabrication (CAS), National Center for Nanoscience and Technology, Beijing 100190, China

[6]State Key Laboratory of Luminescent Materials and Devices, South China University of Technology, Guangzhou 510640, China

[7]Center for Advanced Low-Dimension Materials, Donghua University, Shanghai 201620, China

[8]Laboratory of Organic Electronics, ITN, Linköping University, SE-60174, Norrköping, Sweden

Citation: D Q Li, Y H Zeng, Z Chen, S F Leng, Z Xiao, Q F Xue, T Y Hao, M Lv, H B Wu, L N Lin, J M Yang, Z F Ma, J Q Chen, R Huang, F Liu, H M Zhu, X J Liu, L M Ding, M Fahlman, and Q Y Bao, Investigating the reason for high FF from ternary organic solar cells[J]. *J. Semicond.*, 2021, 42(9), 090501. http://doi.org/10.1088/1674-4926/42/9/090501

SUPPORTING INFORMATION

Materials

The active materials PM6 and Y6 were purchased from Solarmar Materials Inc. EH-IDTBR was supplied by Derthon Optoeletronic Material Science Technology Co., Ltd. Poly-(3,4-ethylenedioxythiophene):poly-(styrenesulphonicacid) (PEDOT:PSS) (Clevios PVP AI 4083) was obtained from H.C. Starck Germany. Aurum (Au) and silver (Ag) were purchased from Alfa Aesar Co., Ltd. All materials were used as received.

Device fabrication and measurements

The organic solar cell devices were fabricated with a conventional configuration of ITO/PEDOT:PSS/active layer/PFN-Br/Ag. The indium tin oxide (ITO)-glass substrates were sequentially washed by Decon dilution solution, deionized water, acetone, absolute ethyl alcohol and isopropyl alcohol using ultrasonic process for each 20 min, respectively. Before preparing the device, the ITO substrates were treated by UV-ozone for 20 min. The PEDOT:PSS was spin-coated at 4000 rpm for 30 s on the cleaned ITO substrate and annealed at 150 °C for 20 min in air. The PEDOT:PSS/ITO substrates were transferred into an N_2-filled glove box for preparing the photoactive layer. The PM6:Y6 blend and PM6:EH-IDTBR blend solutions were prepared using chloroform solvent. The concentration of PM6 in the blend solution is 6.5 mg/mL (donor : accept = 1 : 1.2 by weight), with 0.75% chloronaphthalene (CN) by volume as additive, and stirred for 4 h. The ternary blends were obtained by adjusting the doping ratio of EH-IDTBR in acceptors, which are 0, 5%, 10%, 20%, 30%, 50%, 80%, and 100% by weight. The binary and ternary active layers were obtained by spin-coated on PEDOT:PSS with the thickness of 110 nm, and then annealed at 80 °C for 8 min. After that, the PFN-Br (0.5 mg/mL in methanol) was spin-coated on the top of active layers at 3000 rpm for 30 s to form an electron transporting layer. Finally, the Ag (100 nm) electrode was thermally deposited with a shadow mask with the device area of 0.05 cm^2 at the pressure of 10^{-4} Pa. The current density-voltage characteristics of the solar cells were performed in a glove box filled with nitrogen at room temperature using a programmable Keithley 2400 source measurement unit under simulated solar light of AM 1.5 G (SS-F5-3A, Enlitech). The light intensity was determined by the standardized mono-silicon cell (SRC-2020, Enlitech) at 100 mW/cm^2, calibrated by the National Renewable Energy Laboratory (NREL). The forward scan was adopted to test the *J–V* curves, and the scan step is 0.02 V and the delay time is 1 ms. The scan mode is sweep. The external quantum efficiency (EQE) spectra were obtained by a photo-modulation spectroscopic setup (Newport monochromator). A calibrated silicon detector (PRL-12, Newport, USA) with known photo response was utilized as a reference.

Ultraviolet photoelectron spectroscopy (UPS)

UPS was performed in an ultrahigh vacuum system including a sample analysis chamber with the base pressure of 2×10^{-10} mbar to characterize the vertical ionization potential and the work function. UPS was recorded (Scienta-3000) using a He-discharge lamp with HeI 21.22 eV as excitation source with a resolution of 0.05 eV. The energies of Integer Charge Transfer stares energies were deduced from the work functions of the neat organic films coated on the different substrates with a broad range of the work function.

UV–vis absorption

The Shimadzu spectrometer model UV-1800 was used to obtain the UV–vis absorption spectrum of active layer films on the quartz plates at room temperature.

Steady state photoluminescence (PL) and time-

Danqin Li and Yihan Zeng contributed equally to this work.
Correspondence to: L M Ding, ding@nanoctr.cn; Q Y Bao, qybao@clpm.ecnu.edu.cn
Received 7 JULY 2021.

resolved photoluminescence (TRPL)

PL and TRPL spectra were obtained by the time resolved absorption spectral analysis system, which consist of DTC UNIT M12977-01 (HAMAMATSU, Japan) and a picosecond light pulser C10196 (HAMAMATSU, Japan).

Transient absorption spectroscopy (TAS)

For femtosecond fs-TAS, the fundamental output from Yb:KGW laser (1030 nm, 220 fs Gaussian fit, 100 kHz, Light Conversion Ltd) was separated to two light beam. One was introduced to NOPA (ORPHEUS-N, Light Conversion Ltd) to generate a certain wavelength for pump beam (here we use 725 nm), the other was focused onto a YAG plate to produce white light continuum as probe beam. The pump and probe overlapped on the sample at a small angle less than 10°. The transmitted probe light from sample was collected by a linear charge-coupled device (CCD) array.

Space charge limited current measurement

Space charge limited current (SCLC) measurement was applied to determine the electron and hole mobilities using the electron-only device ITO/ZnO/active layer/PFN-Br/Ag and hole-only device ITO/PEDOT:PSS/active layer/Au, respectively. The mobility (μ) was calculated by fitting the SCLC with the Motto-Gurney law[1]:

$$J = \frac{9}{8}\mu\varepsilon_r\varepsilon_0\left(V^2/L^3\right), \tag{S1}$$

where J is the current density, ε_0 is the permittivity of free space, ε_r is the relative permittivity of the materials, V is the applied voltage, and L is the active layer thickness.

Transient photovoltage (TPV) and transient photocurrent (TPC) measurement

TPV and TPC were adopted to gain the lifetime of carriers and carrier density. The background illumination was provided by a normal LED light source, and pulsed light was provided by arbitrary wave generator (AFG322C, Tektronix). The photovoltage traces were registered by the oscilloscope (AFG322C, Tektronix). The data are analyzed and derived as follows:

Voltage decay in TPV acquired by using 1 MΩ input impedance of oscilloscope is given by the equation:

$$\Delta V = \Delta V_0 \exp\left(\frac{-t}{\tau}\right), \tag{S2}$$

where τ is carrier lifetime and Δ is the amplitude of TPV transient under different illumination condition.

TPV decay lifetime is found to follow an exponential dependence on V_{OC}:

$$\tau = \tau_{\Delta V}\exp(-\beta V_{OC}), \tag{S3}$$

$\tau_{\Delta V}$ represents the decay-time prefactor.

Current decay in TPC acquired across a 50 Ω resistor connected to 1 MΩ input impedance of oscilloscope is given by

$$\Delta I = \Delta I_0 \exp\left(\frac{-t}{\tau_{tpc}}\right), \tag{S4}$$

where τ_{tpc} is carrier extraction time and ΔI_0 is the amplitude of TPC transient under different illumination condition

In TPC measurements, the total charges ΔQ generated by the pulse laser can be calculated by integrating the transient photocurrent over time

$$\Delta Q = \int I\mathrm{d}t. \tag{S5}$$

Combined with the TPV and TPC, differential capacitance can be calculated by

$$C = \frac{\Delta Q}{\Delta V_0}. \tag{S6}$$

Corresponding differential capacitance values follow the exponential dependence on the open-circuit voltage

$$C = C_0\exp\left(-\gamma V_{OC}\right) + D. \tag{S7}$$

The charge carrier density (n) under certain illumination condition is given by treating the device as a parallel-plate capacitor and integrating with respect to voltage

$$n = \frac{1}{qAL}\int_{-\infty}^{V_{OC}} C_0\exp\left(\gamma V\right)\mathrm{d}V, \tag{S8}$$

where A represent the area of the device and L is the thickness.

By using these parameters obtained, the TPV decay lifetime under different carrier densities follow a power law with order λ,

$$\tau \propto n^{-\lambda}. \tag{S9}$$

Corresponding charge-carrier recombination follow the rate equation

$$\frac{\mathrm{d}n}{\mathrm{d}t} \propto -n^{\lambda+1}, \tag{S10}$$

where λ + 1 represents the reaction order of recombination. The non-geminate recombination rate coefficient K_{nge} is obtained as $K_{nge} = \frac{1}{\tau n}$.

Highly sensitive EQE (sEQE) measurement

The halogen light source (LSH-75, Newport) passed through the monochromator (CS260-RG-3-MC-A, Newport) to form monochromatic light. The signals were finally collected by the front-end current amplifier (SR570, Stanford) and phase-locked amplifier (Newport), thus the sEQE spectrum can be acquired. In this process, a corrected Si solar cell (S1337-1010BR) served as a standard detector.

Electroluminescence (EL) measurement

EL spectrum measurement was conducted by direct-current meter (PWS2326, Tectronix) to provide bias voltage for device measurement, and the luminescence signal was collected by the fluorescence spectrometer (KYMERA-328I-B2, Andor technology LTD).

EQE-EL measurement

The test system was composed of Keithley 2400 digital source meter, Keithley 6482 picometers and a standard Si solar cell.

$$\mathrm{EQE}_{PV,CT}(E) = \frac{f}{E\sqrt{4\pi\lambda k_B T}}\exp\left(\frac{-(E_{CT}+\lambda-E)^2}{4\lambda k_B T}\right), \tag{S11}$$

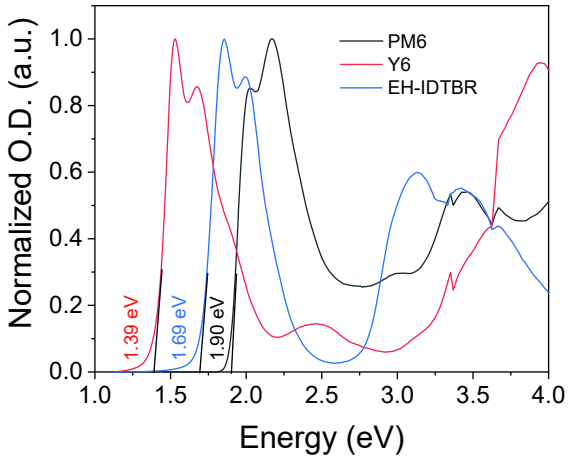

Fig. S1. Tauc plots for PM6, Y6 and EH-IDTBR films.

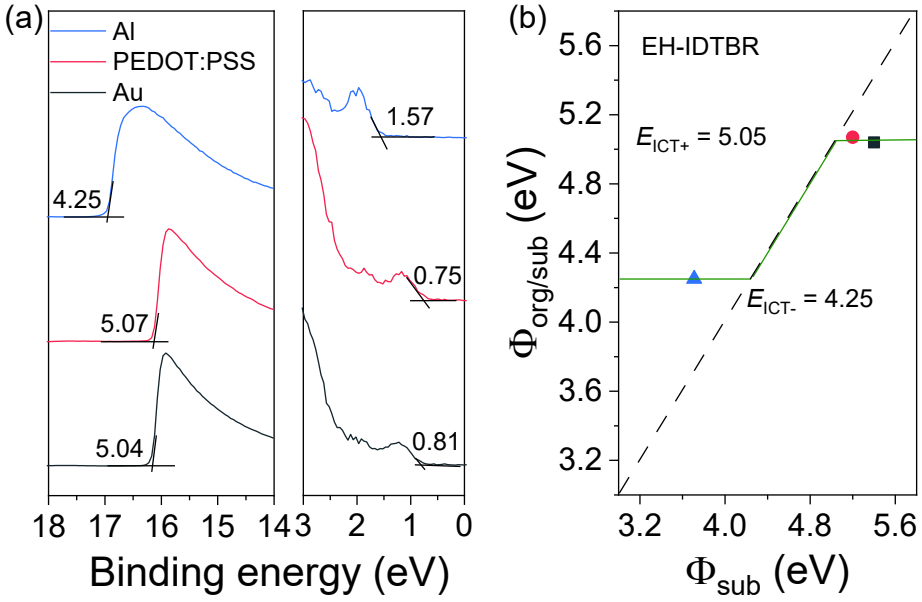

Fig. S2. (a) UPS spectra of EH-IDTBR film on different substrates. (b) Energies of ICT states of EH-IDTBR film.

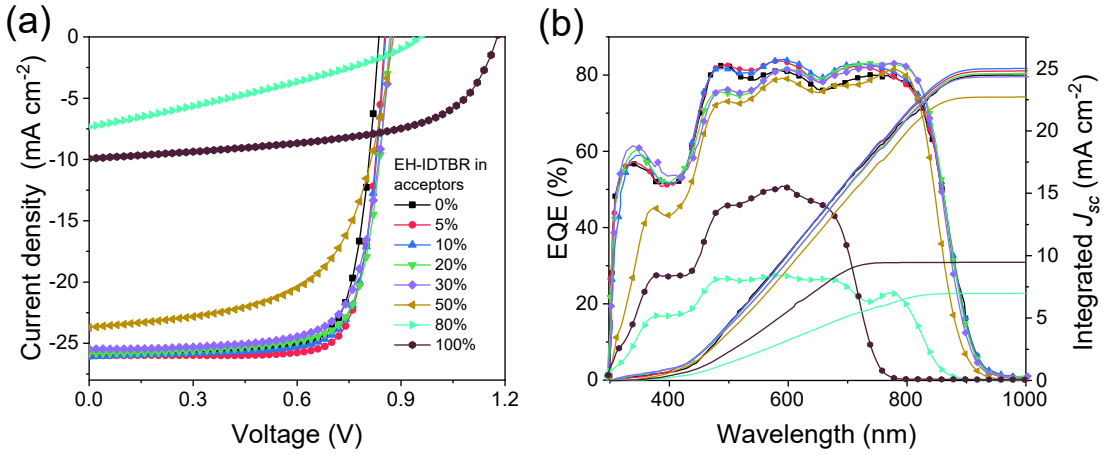

Fig. S3. (Color online) (a) *J*–*V* curves of ternary cells with different EH-IDTBR contents; (b) the corresponding EQE curves.

$$\mathrm{EQE}_{\mathrm{EL,CT}}(E) = E\frac{f}{\sqrt{4\pi\lambda k_{\mathrm{B}}T}}\exp\left(\frac{-(E_{\mathrm{CT}}-\lambda-E)^2}{4\lambda k_{\mathrm{B}}T}\right), \quad \text{(S12)}$$

$$\mathrm{EQE}_{\mathrm{PV}}(E) \propto EL(E)E^{-2}\exp\left(\frac{E}{k_{\mathrm{B}}T}\right), \quad \text{(S13)}$$

where T was absolute temperature, k_{B} was Boltzmann's con-

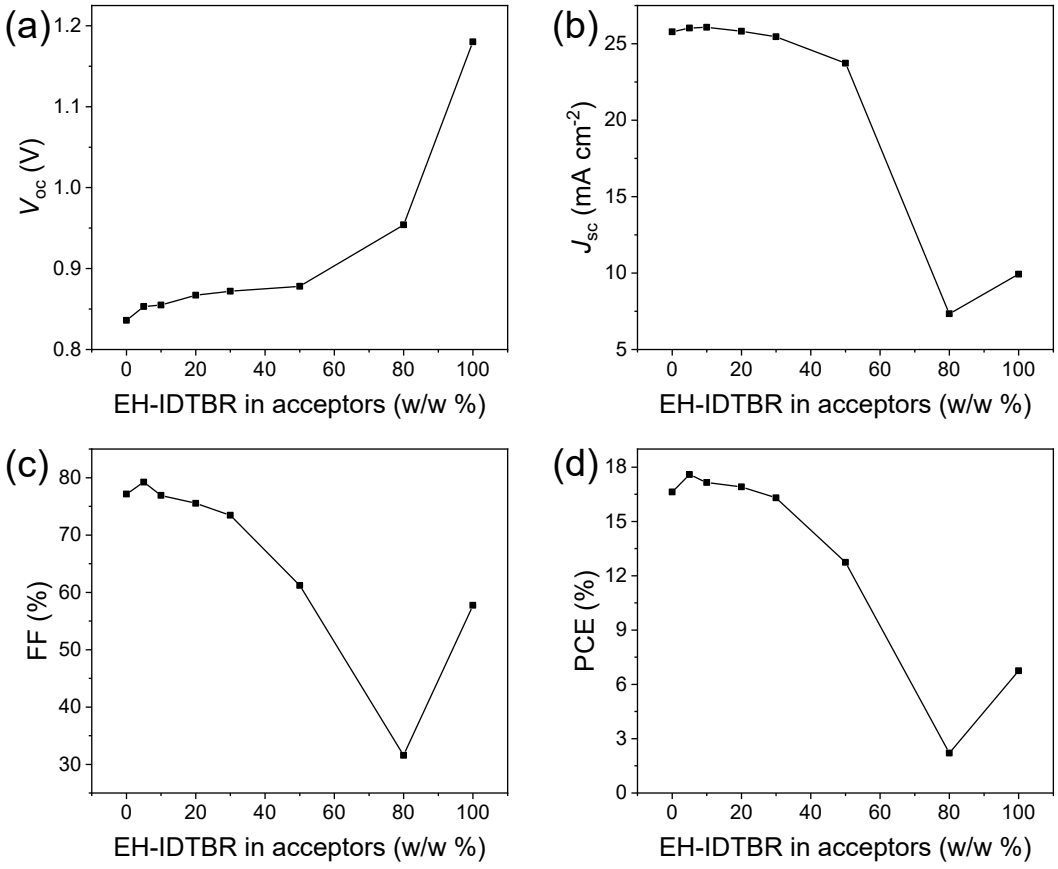

Fig. S4. (a) V_{oc}, (b) J_{sc}, (c) FF and (d) PCE of the ternary cells with different EH-IDTBR contents.

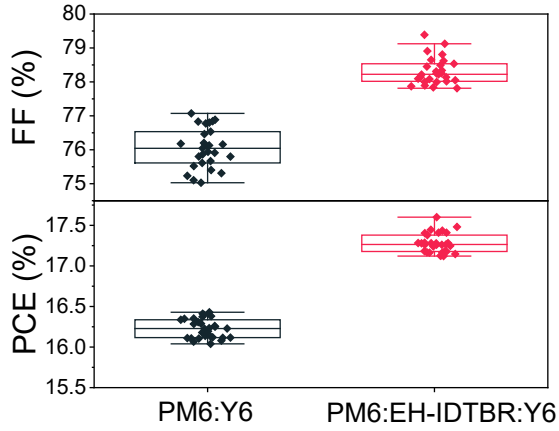

Fig. S5. FF and PCE distribution for PM6:Y6 and PM6:EH-IDTBR:Y6 cells.

stant and E represented photon energy. For the fit parameters, E_{CT} represented the free-energy difference between the charge transfer complex (CTC) ground state and the CT excited state, and E_{CT} energy can be quantified by the point of intersection between CT absorption and emission. λ was the reorganization energy associated with the CT absorption process, and f was a measure of the strength of the donor–acceptor coupling.

The total loss can be divided into charge extraction (E_g to E_{CT}) and recombination (E_{CT} to V_{OC}) losses. The recombination losses can be quantified using Eq. (S14), including the contribution of radiative (ΔV_{rad}) and non-radiative losses ($\Delta V_{non\text{-}rad}$). Employing the Marcus fitting parameters f, λ, and E_{CT}, which are extracted from Fig. 1(g) and Fig. S24 and summarized in Table S6, the ΔV_{rad} can be quantified using Eq. (S15). ΔV_{norad} can be directly evaluated according Eq. (S16) by EQE_{EL} measurements. The calculated value of ΔV_{rad} and $\Delta V_{non\text{-}rad}$ for all our devices can be seen in Table S7. Consequently, the total energy loss followed the expression in Eq. (S17).

$$\Delta V_{rad} + \Delta V_{non\text{-}rad} = E_{CT} - eV_{OC}, \tag{S14}$$

$$\Delta V_{rad} = -KT\ln\left(\frac{J_{SC}h^3c^2}{fq2\pi(E_{CT}-\lambda)}\right), \tag{S15}$$

$$\Delta V_{non\text{-}rad} = -KT\ln(EQE_{EL}) \tag{S16}$$

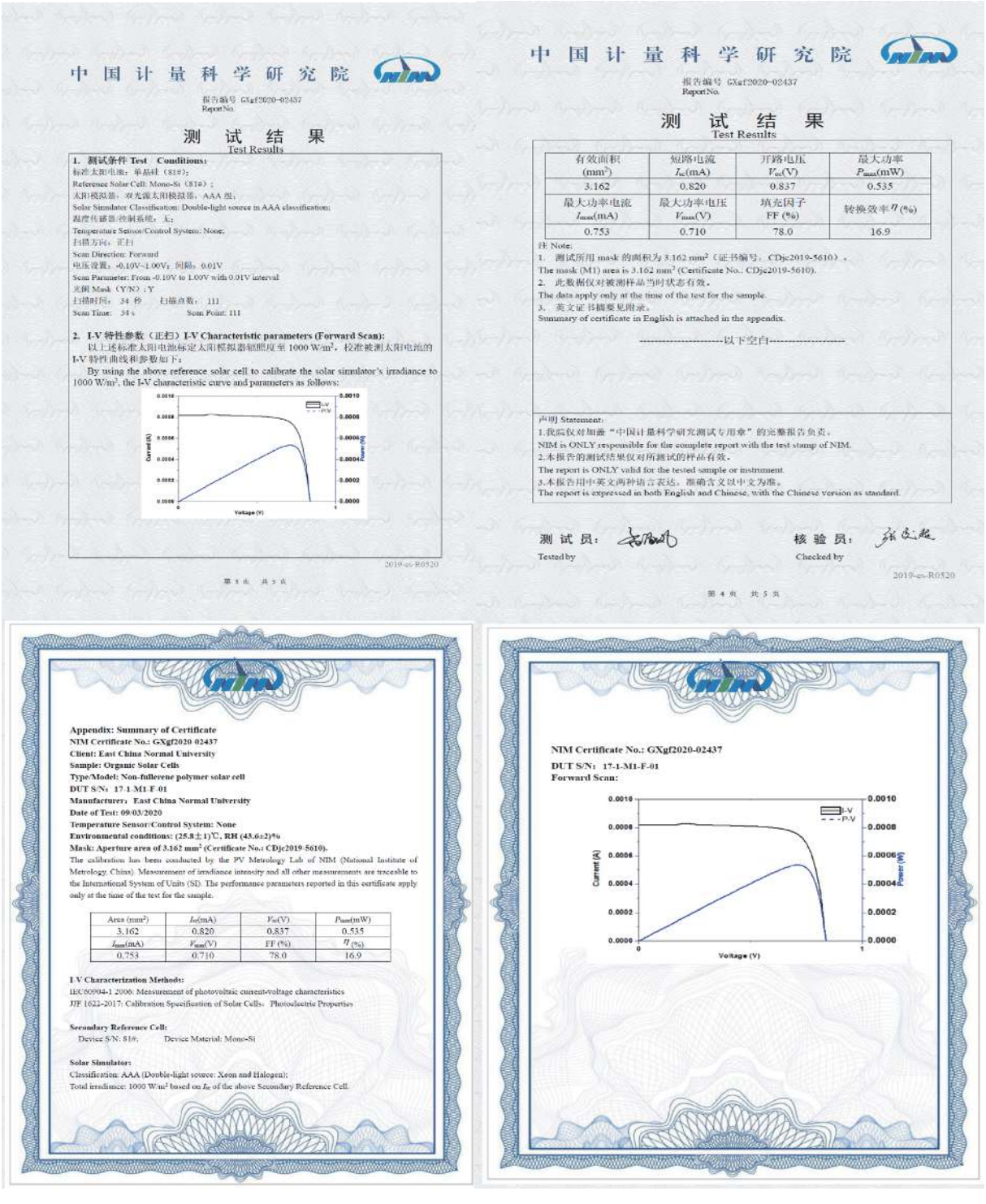

Fig. S6. (Color online) NIM (Beijing) report for PM6:EH-IDTBR:Y6 cells. (V_{oc}: 0.837 V, J_{sc}: 25.93 mA/cm^2, FF: 78%, PCE: 16.9%)

$$E_{loss} = E_g - qV_{OC} = (Eg - E_{CT}) + \left[-KT\ln\left(\frac{J_{SC}h^3c^2}{fq2\pi\,(E_{CT}-\lambda)}\right)\right] + [-KT\ln(EQE_{EL})]. \quad \text{(S17)}$$

Morphology characterization

Atomic force microscopy (AFM) measurements were carried out in the tapping mode (Mutimode 8, Bruker) at ambient condition. Transmission electron microscope (TEM) measurements were conducted with a JEM-2100F microscope operated at 150 K. GIWAXS measurements were accomplished with a Xeuss 2.0 SAXS/WAXS laboratory beamline using a Cu X-ray source (8.05 keV, 1.54 Å) and a Pilatus3R 300K detector. The incidence angle is 0.2°. The parameters of π–π stacking distance (*d*-spacing) and the crystal size of the domains can be estimated by crystal coherence length (CCL), according to the Scherrer equation[2]:

$$d\text{-spacing} = \frac{2\pi}{q}, \quad \text{(S18)}$$

$$\text{CCL} = 0.9 \times \frac{2\pi}{\text{FWHM}}. \quad \text{(S19)}$$

Here, q is the location of the peak and FWHM is the half-

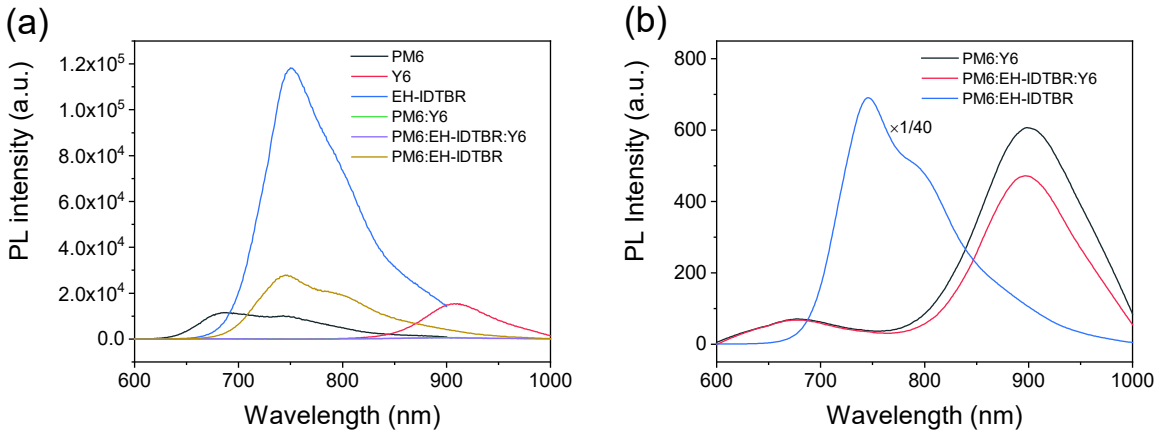

Fig. S7. (a) PL spectra of neat and blend films. (b) Enlarged PL spectra of blend films.

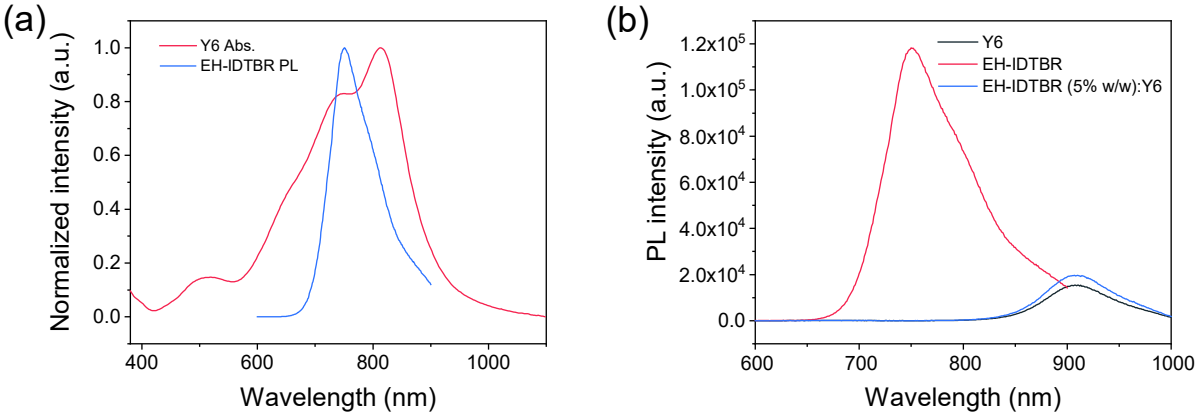

Fig. S8. (a) UV–vis absorption spectrum of Y6 and PL spectrum of EH-IDTBR. (b) PL spectra of Y6, EH-IDTBR and EH-IDTBR (5% w/w):Y6 films.

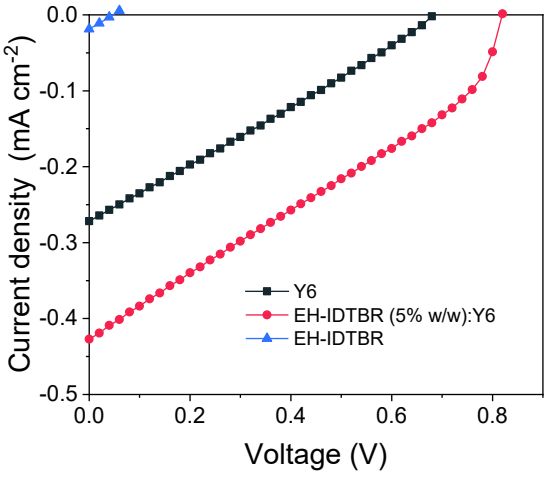

Fig. S9. *J*–*V* curves of the cells with Y6, EH-IDTBR and EH-IDTBR (5% w/w):Y6 as active layers, respectively.

width at the diffraction peak.

Femtosecond (fs) transient absorption (TA) spectroscopy therefore is employed to probe the hole transfer dynamics in the ternary and reference binary blends. A 725 nm wavelength laser is applied to selectively excite the acceptors without pumping the donor. For the acceptor films, the bleach peaks mainly appear at 830 nm for Y6 and EH-IDTBR (5% w/w):Y6, 680 nm for EH-IDTBR (Fig. S10), corresponding to the ground state bleach (GSB) and stimulated emission (SE) of the absorption transition in the acceptors after photoexcitation[3, 4]. Figs. S11(a) and S11(b) display the 2D color plot and a few representative TA spectra for the ternary PM6:EH-IDTBR (5% w/w):Y6 film, respectively. The main bleach signals at 650-850 nm appear from the EH-IDTBR (5% w/w):Y6. With the decay of the EH-IDTBR (5% w/w):Y6 bleach peaks, a few clear bleach peaks emerge at 550–610 nm, which match well with the absorption features of PM6. These GSBs in the donor rise with the bleach decay process in the acceptors

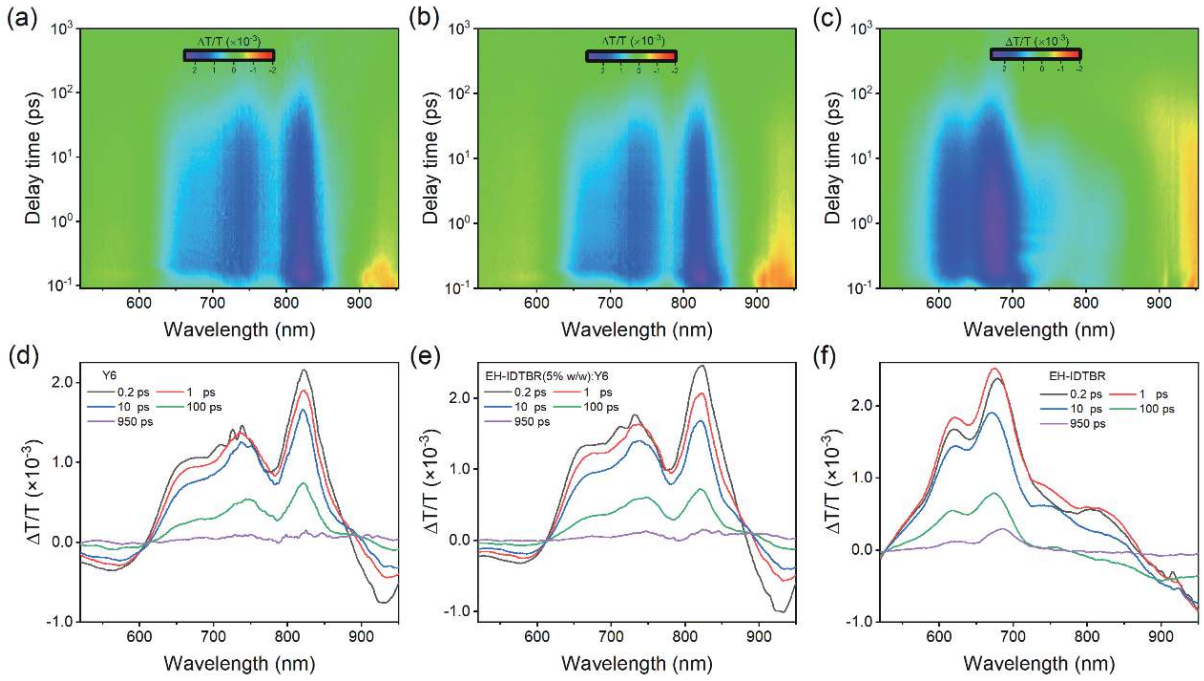

Fig. S10. (Color online) 2D color plots of fs TA spectra for (a) Y6, (b) EH-IDTBR(5%):Y6 and (c) EH-IDTBR films under 725 nm excitation; (d–f) the corresponding representative TA spectra at indicated delay time.

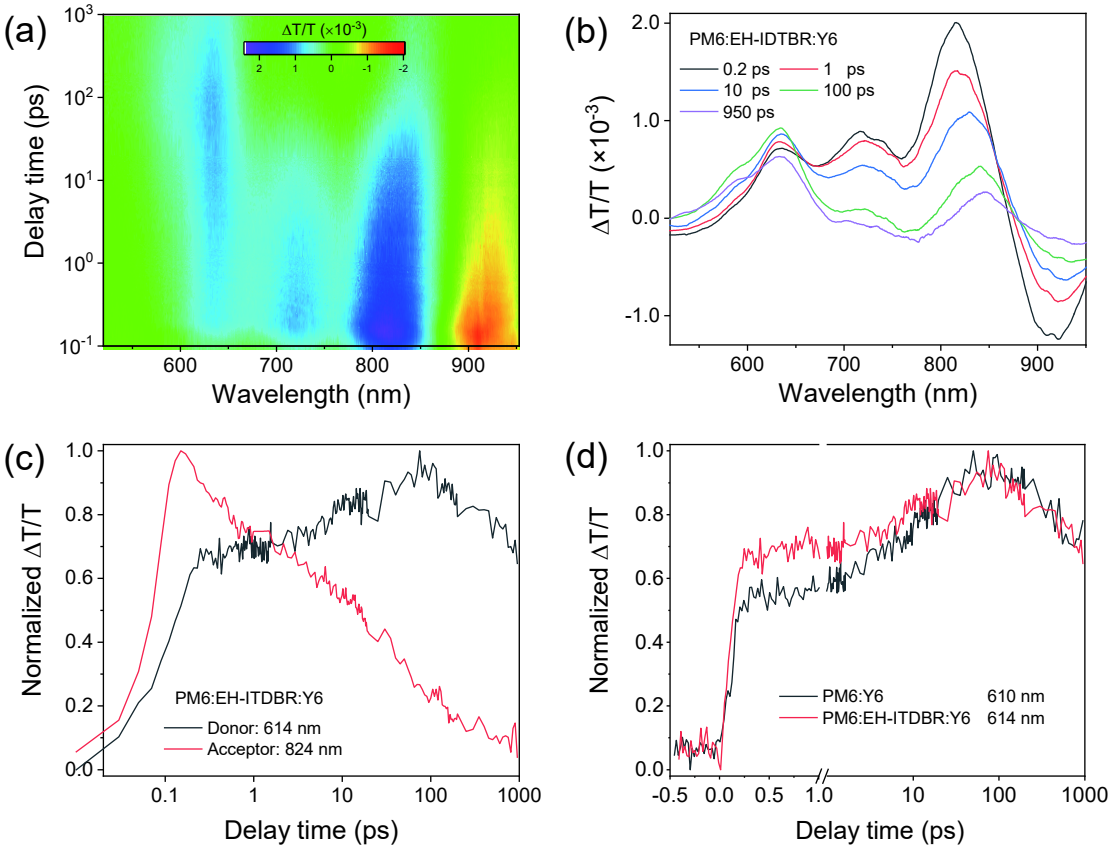

Fig. S11. (Color online) (a) 2D color plots of fs TA spectra for PM6:EH-IDTBR:Y6 blend film at under 725 nm excitation with a fluence below 10 μJ/cm^2. (b) Representative fs TA spectra at indicated delay times. (c) TA hole transfer kinetics in PM6:EH-IDTBR:Y6. (d) Comparison of the hole transfer kinetics for PM6:Y6 (black line) and PM6:EH-IDTBR:Y6 (red line).

(Fig. S11(c)), confirming the effective hole transfer process at the donor/acceptor interface[5, 6]. The similar TA spectra and hole transfer process can be observed in the reference two binary PM6:Y6 and PM6:EH-IDTBR blends (Fig. S12). As shown in Fig. S11(d) and Fig. S12(f), we select the representative kinetics wavelength where the acceptors show no TA signal (Fig. S10) to monitor rising kinetics of PM6. The hole-transfer rates are fitted with bi-exponential functions with time constants

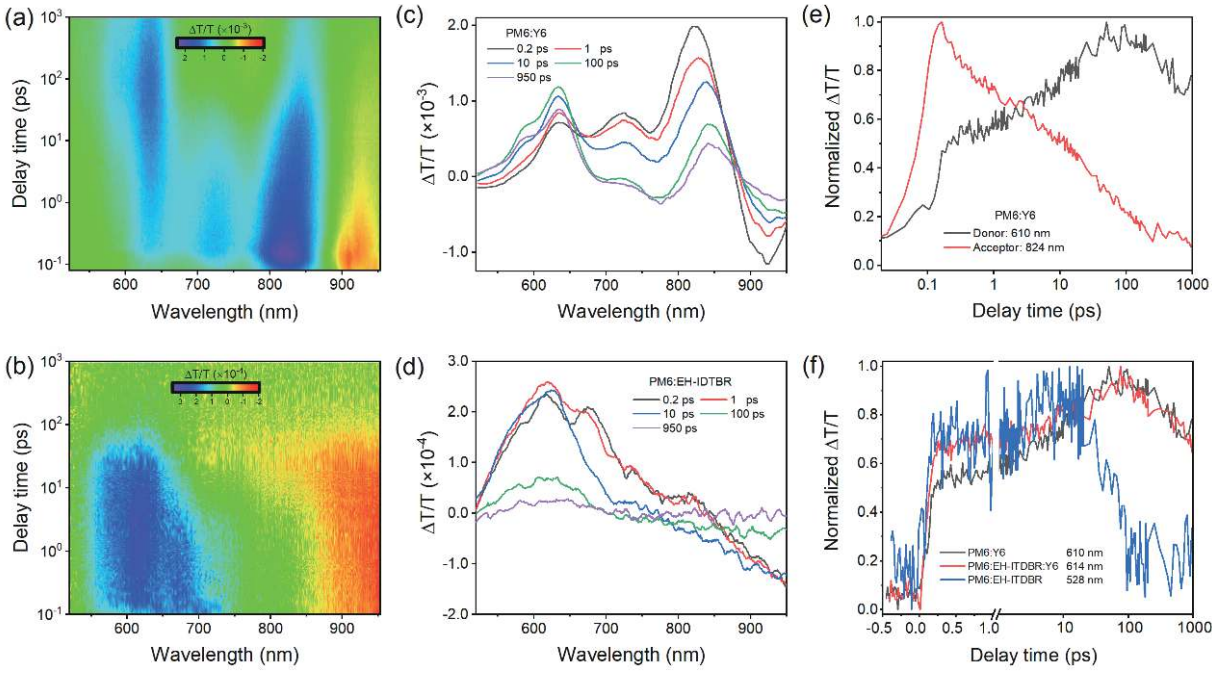

Fig. S12. (Color online) 2D color plots of fs TA spectra for (a) PM6:Y6 and (b) PM6:EH-IDTBR blend films under 725 nm excitation; representative fs TA spectra of (c) PM6:Y6 and (d) PM6:EH-IDTBR films at indicated delay times; (e) TA hole transfer kinetics in PM6:Y6 showing the hole transfer process; (f) comparison of the hole transfer kinetics for PM6:Y6 (black line), PM6:EH-IDTBR:Y6 (red line) and PM6:EH-IDTBR (blue line).

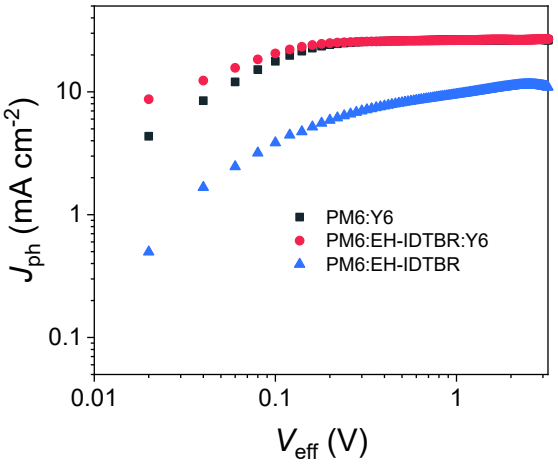

Fig. S13. J_{ph}–V_{eff} plots for PM6:Y6, PM6:EH-IDTBR and PM6:EH-IDTBR:Y6 cells.

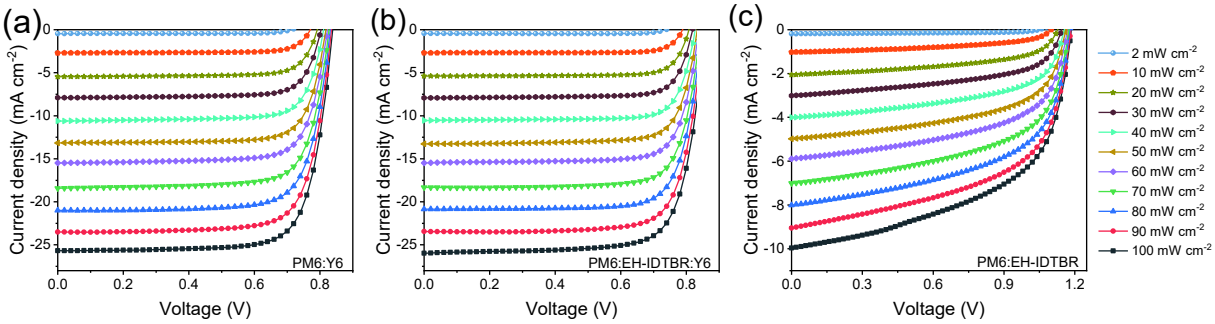

Fig. S14. (Color online) *J*–*V* curves of PM6:Y6, PM6:EH-IDTBR:Y6 and PM6:EH-IDTBR cells under different illumination intensities.

of $\tau_{1,\,h}$ = 119 fs and $\tau_{2,\,h}$ = 13.11 ps for the PM6:Y6 blend. The former represents the ultrafast exciton dissociation at the donor/acceptor interface, while the latter is assigned to the exciton diffusion time towards interface before dissociation[5, 7]. As a contrast, the ternary blend exhibits the faster transfer rate with time constants of $\tau_{1,\,h}$ = 88 fs and $\tau_{2,\,h}$ = 10.41 ps. The trend in the hole transfer rate is consistent with the values of HOMO offsets. Introducing EH-IDTBR into the PM6:Y6

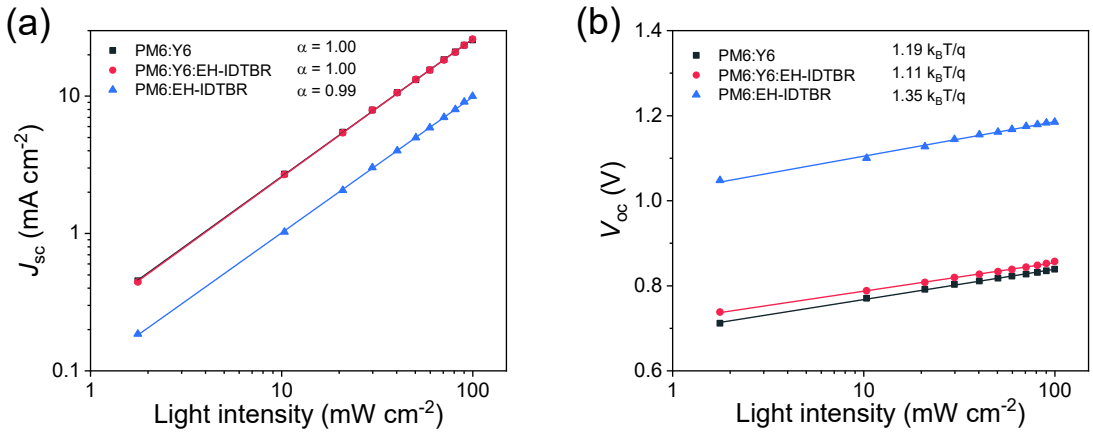

Fig. S15. (a) J_{sc}–P_{light} and (b) V_{oc}–P_{light} plots for PM6:Y6, PM6:EH-IDTBR:Y6 and PM6:EH-IDTBR cells.

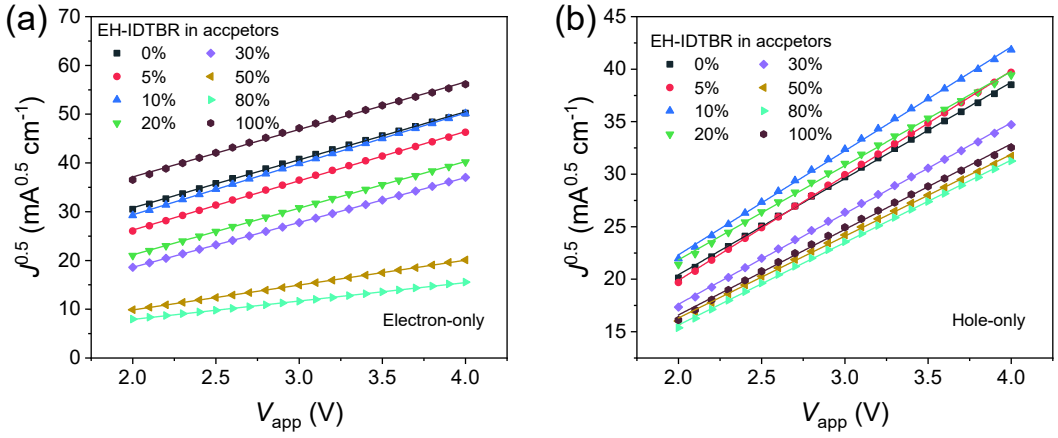

Fig. S16. $J^{0.5}$–V_{app} plots for (a) the electron-only devices with a structure of ITO/ZnO/active layer/PFN-Br/Ag and (b) the hole-only devices with the structure of ITO/PEDOT:PSS/active layer/Au.

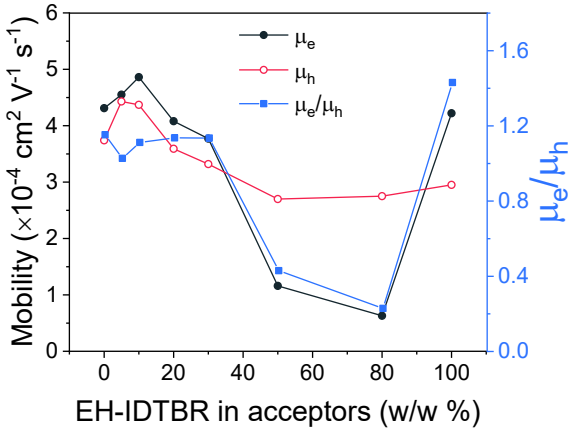

Fig. S17. The variation of μ_e, μ_h and μ_e/μ_h along with EH-IDTBR contents.

blend increases the size of the donor/acceptor HOMO offset, leading to the enhanced driving force with the faster hole transfer, contributing to the enhanced J_{sc} and FF in the ternary OSCs. Although the PM6:EH-IDTBR blend has the largest HOMO offset with the fastest hole transfer speed (Fig. S12(f)), the signal intensity rapidly decreases from 10 to 100 ps, which signifies the sharp recombination process and thus results in the poor device performance.

The charge carrier lifetime (τ) is derived from TPV that corresponds to the different V_{oc} (Figs. S18(a)–S18(c)) by mono-exponential fitting of TPV decay and shows the linear dependence on V_{oc} in semi-log plot[8, 9] (Fig. S19(a)). We find that the introduction of EH-IDTBR (5% w/w) yields a longer lifetime (τ = 6.54 μs) under 1 sun illumination compared with the binary devices (τ = 3.46 μs for PM6:Y6, and τ = 1.46 μs for PM6:EH-IDTBR). The charge carrier density (n) is extracted from the differential capacitance approximation based on both TPC and TPV results[10, 11] (Described in Experimental section, and Figs. S18(d)–S18(f)). Besides, the devices follow a power law: $\tau = \tau_0 n^{-\lambda}$ (where τ_0 is the constant, λ represents

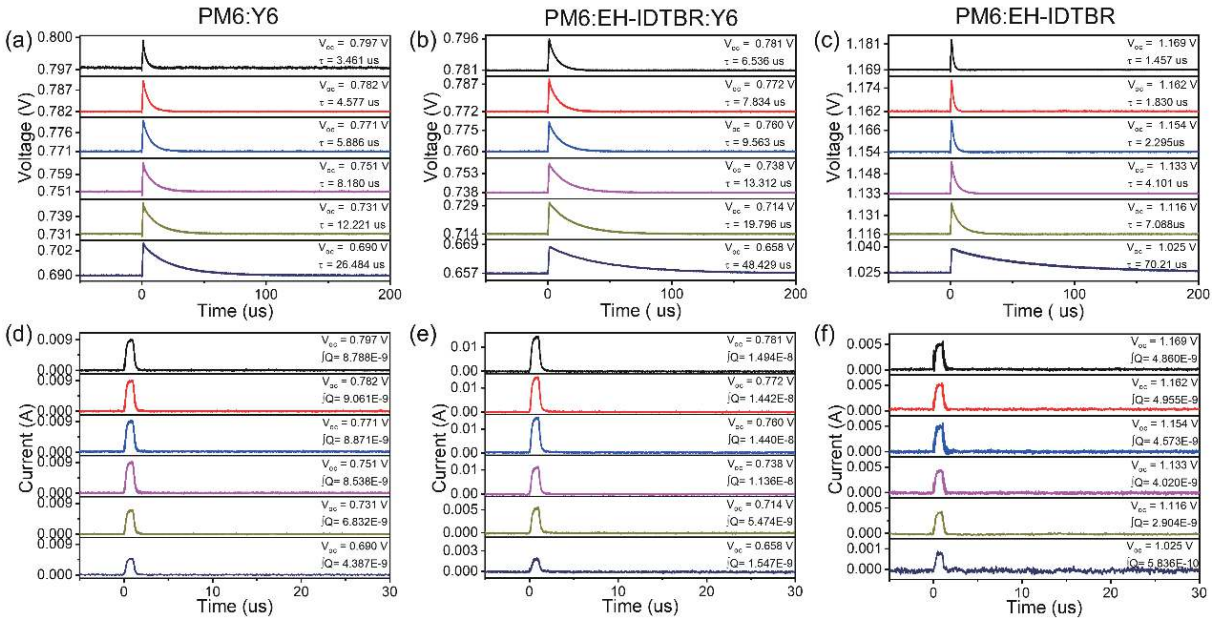

Fig. S18. (a–c) TPV and (d–f) TPC spectra for PM6:Y6, PM6:EH-IDTBR:Y6 and PM6:EH-IDTBR cells under different light intensities.

the recombination exponent)[12, 13]. A recombination order $R = \lambda + 1$ equal to 2 suggests dominant biomolecular recombination process[12]. The R of 1.99 for the optimal ternary device means nearly an ideal (trap-free) bimolecular recombination, justified by the high FF of 79.22%. The R greater than 2 is normally attributed to the effect of trap-assisted recombination. For binary PM6:Y6 and PM6:EH-IDTBR devices, the R are 2.06 and 2.35, respectively, in line with the results of steady-state dependence of V_{oc} on light density (Fig. 1(f)). The non-geminate recombination rate coefficient (K_{nge}) is defined by $1/\tau_{(n)}n$ (where $\tau_{(n)}$ is the charger carrier lifetime under corresponding density)[8, 10]. As shown in Fig. S19(d), the ternary device has the lowest K_{nge} of 1.14×10^{-17} m^3/s, confirming the suppressed recombination. As K_{nge} and charge mobility follow the same dependence on n, the Langevin recombination rate coefficient (K_L) can be assessed by $\frac{q}{\varepsilon_0 \varepsilon_s}(u_e + u_h)$[14]. The K_L for the ternary and PM6:Y6 binary are 5.41×10^{-16} and 4.86×10^{-16} m^3/s, respectively, as included in Fig. S19(d) for comparison. The K_{nge} of the optimized ternary device is smaller than the $K_{L,}$ indicating significantly reduced non-geminate recombination loss.

The root-mean-square roughnesses are slightly varied, indicating that EH-IDTBR is finely mixed with the host PM6:Y6 blend. As seen from their phases images, the PM6:EH-IDTBR (5% w/w):Y6 blend features a uniform fibrillar structure, similar with the PM6:Y6.

The E_g of the blend films calculated by the intersection point of absorption and emission spectra are 1.415, 1.416 and 1.721 eV for PM6:Y6, PM6:EH-IDTBR:Y6 and PM6:EH-IDTBR, respectively (Fig. S24). The E_{CT} is determined by fitting the sub-gap absorption of highly sensitive EQE and EL[15]. ΔE_{rad} is inevitable in the devices, and the ΔE_{rad} of the ternary device is close to the host binary PM6:Y6 device since there is no additional gap states after introducing EH-IDTBR. $\Delta E_{non\text{-}rad}$ is quantified by EQE_{EL} measurements, expressed as $-kT\ln(EQE_{EL})$[16].

References

[1] Matsushima T, Bencheikh F, Komino T, et al. High performance from extraordinarily thick organic light-emitting diodes. Nature, 2019, 572, 502

[2] Du X, Yuan Y, Zhou L, et al. Delayed fluorescence emitter enables near 17% efficiency ternary organic solar cells with enhanced storage stability and reduced recombination energy loss. Adv Funct Mater, 2020, 30, 1909837

[3] Li S, Zhan L, Jin Y, et al. Asymmetric electron acceptors for high-efficiency and low-energy-loss organic photovoltaics. Adv Mater, 2020, 32, 2001160

[4] Zhou Z, Liu W, Zhou G, et al. Subtle molecular tailoring induces significant morphology optimization enabling over 16% efficiency organic solar cells with efficient charge generation. Adv Mater, 2020, 32, 1906324

[5] Zhang J, Liu W, Zhou G, et al. Accurate determination of the minimum homo offset for efficient charge generation using organic semiconducting alloys. Adv Energy Mater, 2019, 10, 1903298

[6] Qiu B, Chen Z, Qin S, et al. Highly efficient all-small-molecule organic solar cells with appropriate active layer morphology by side chain engineering of donor molecules and thermal annealing. Adv Mater, 2020, 32, 1908373

[7] Wang D, Qin R, Zhou G, et al. High-performance semitransparent organic solar cells with excellent infrared reflection and see-through functions. Adv Mater, 2020, 32, 2001621

[8] Liu S, Liang Q, Yan J, et al. Distinguishing limits on the fill factor in organic solar cells processed from different solvents: Charge recombination kinetics vs. charge extraction. Org Electron, 2018, 59, 427

[9] Huo M M, Hu R, Zhang Q S, et al. Morphology and carrier non-geminate recombination dynamics regulated by solvent additive in polymer/fullerene solar cells. RSC Adv, 2020, 10, 23128

[10] Wood S, Blakesley J C, Castro F A. Assessing the validity of transient photovoltage measurements and analysis for organic solar cells. Phys Rev Appl, 2018, 10, 024038

[11] Shuttle C G, O'Regan B, Ballantyne A M, et al. Experimental determination of the rate law for charge carrier decay in a polythiophene: Fullerene solar cell. Appl Phys Lett, 2008, 92, 093311

[12] Gasparini N, Jiao X, Heumueller T, et al. Designing ternary blend bulk heterojunction solar cells with reduced carrier recombina-

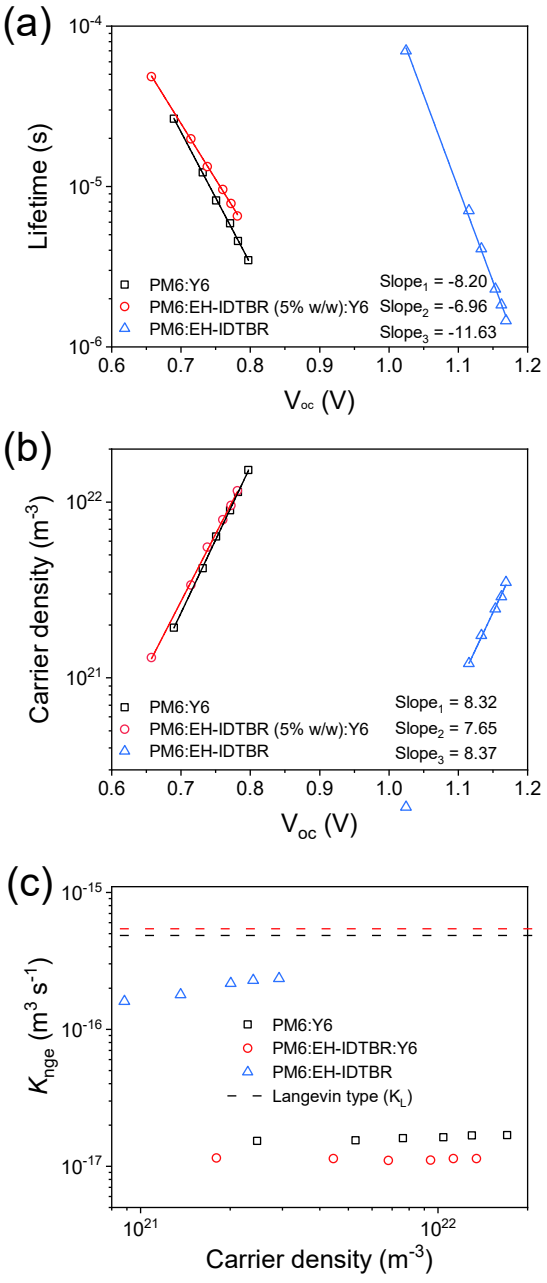

Fig. S19. Characteristics of (a) charge carrier lifetime versus open-circuit voltage and (b) charge carrier density versus open-circuit voltage for PM6:Y6, PM6:EH-IDTBR:Y6 and PM6:EH-IDTBR cells. (c) Non-geminate recombination rate constants for the cells.

tion and a fill factor of 77%. Nat Energy, 2016, 1, 1

[13] Kim J H, Sin D H, Kim H, et al. Improved charge transport and reduced non-geminate recombination in organic solar cells by adding size-selected graphene oxide nanosheets. ACS Appl Mater Interfaces, 2019, 11, 20183

[14] Armin A, Subbiah J, Stolterfoht M, et al. Reduced recombination in high efficiency molecular nematic liquid crystalline: Fullerene solar cells. Adv Energy Mater, 2016, 6, 1600939

[15] Karki A, Vollbrecht J, Dixon A L, et al. Understanding the high performance of over 15% efficiency in single-junction bulk heterojunction organic solar cells. Adv Mater, 2019, 31, 1903868

[16] Karki A, Vollbrecht J, Gillett A J, et al. Unifying charge generation, recombination, and extraction in low-offset non-fullerene acceptor organic solar cells. Adv Energy Mater, 2020, 10, 2001203

[17] Zhang W, Huang J, Xu J, et al. Phthalimide polymer donor guests enable over 17% efficient organic solar cells via parallel-like ternary and quaternary strategies. Adv Energy Mater, 2020, 10, 2001436

[18] Yan C, Tang H, Ma R, et al. Synergy of liquid-crystalline small-molecule and polymeric donors delivers uncommon morphology evolution and 16.6% efficiency organic photovoltaics. Adv Sci, 2020, 7, 2000149

[19] Li D, Zhu L, Liu X, et al. Enhanced and balanced charge transport boosting ternary solar cells over 17% efficiency. Adv Mater, 2020, 32, 2002344

[20] Xie G, Zhang Z, Su Z, et al. 16.5% efficiency ternary organic photovoltaics with two polymer donors by optimizing molecular arrangement and phase separation. Nano Energy, 2020, 69, 104447

[21] Han J, Wang X, Huang D, et al. Employing asymmetrical thieno[3,4-d]pyridazin-1(2h)-one block enables efficient ternary polymer solar cells with improved light-harvesting and morphological properties. Macromolecules, 2020, 53, 6619

[22] Ma Q, Jia Z, Meng L, et al. Promoting charge separation resulting in ternary organic solar cells efficiency over 17.5%. Nano Energy, 2020, 78, 105272

[23] Song J, Li C, Zhu L, et al. Ternary organic solar cells with effi-

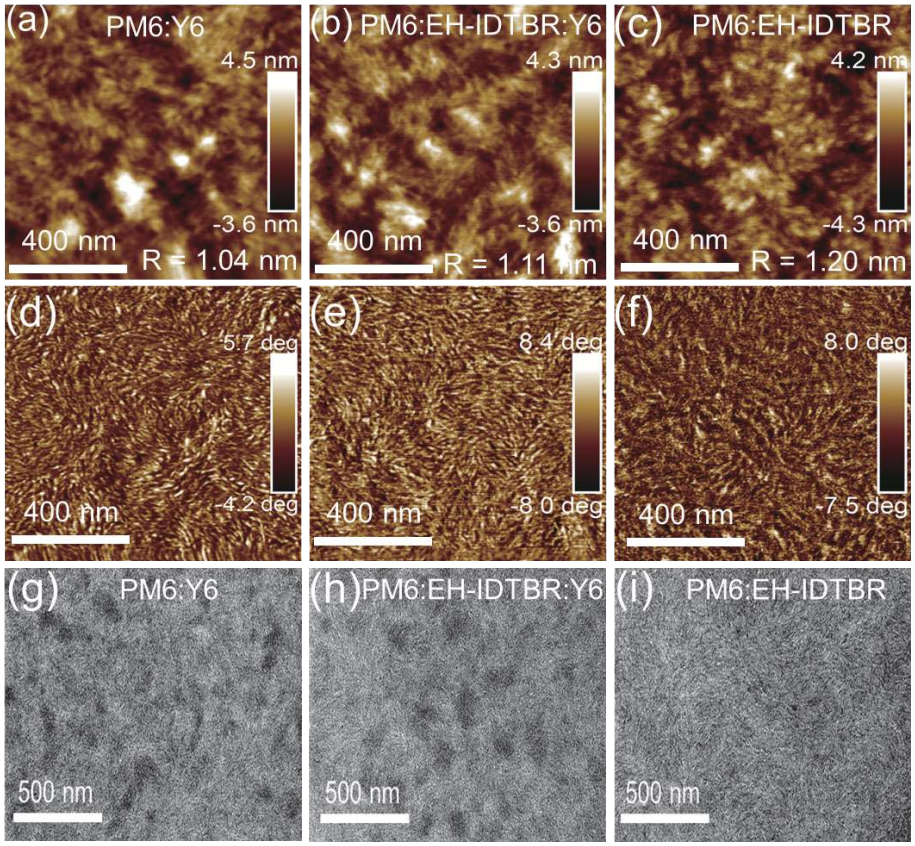

Fig. S20. (Color online) (a–c) AFM height images and (d–f) phase images. (g–i) TEM images.

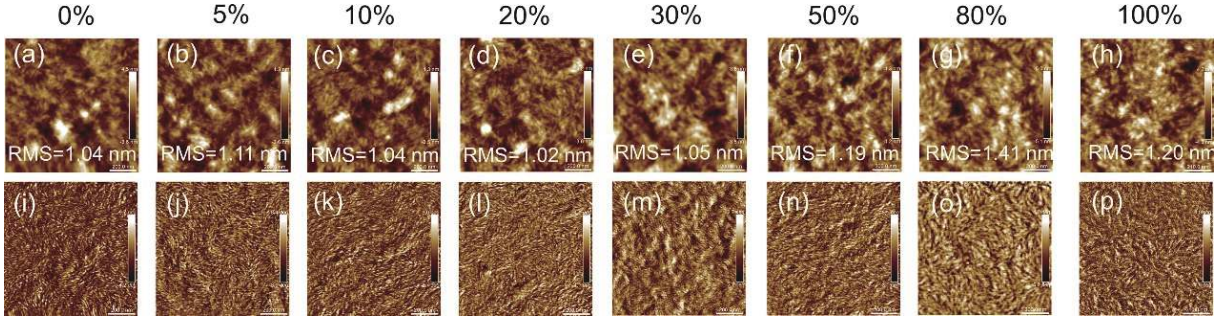

Fig. S21. (Color online) (a–h) AFM height images and (i–p) phase images for the blend films with different EH-IDTBR contents.

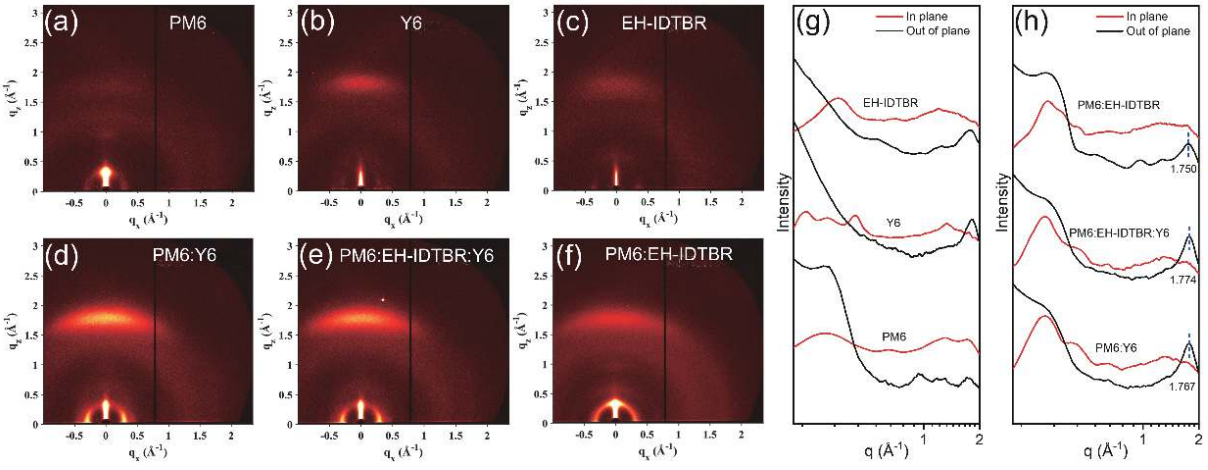

Fig. S22. (Color online) (a–f) 2D GIWAXS patterns of the neat, binary and ternary films. (g–h) In-plane (red) and out-of-plane (black) profiles of the 2D data.

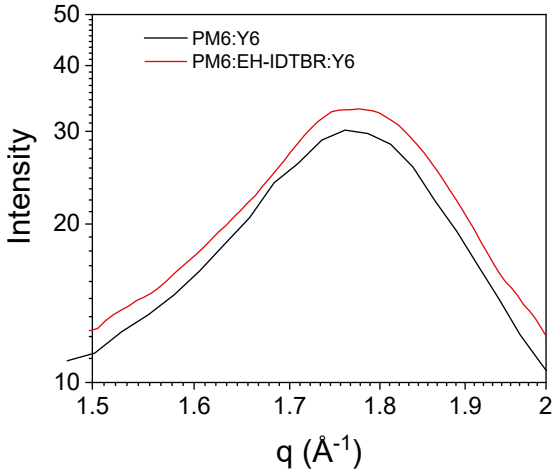

Fig. S23. Enlarged out-of-plane profiles of PM6:Y6 and PM6:EH-IDTBR:Y6 of the 2D data.

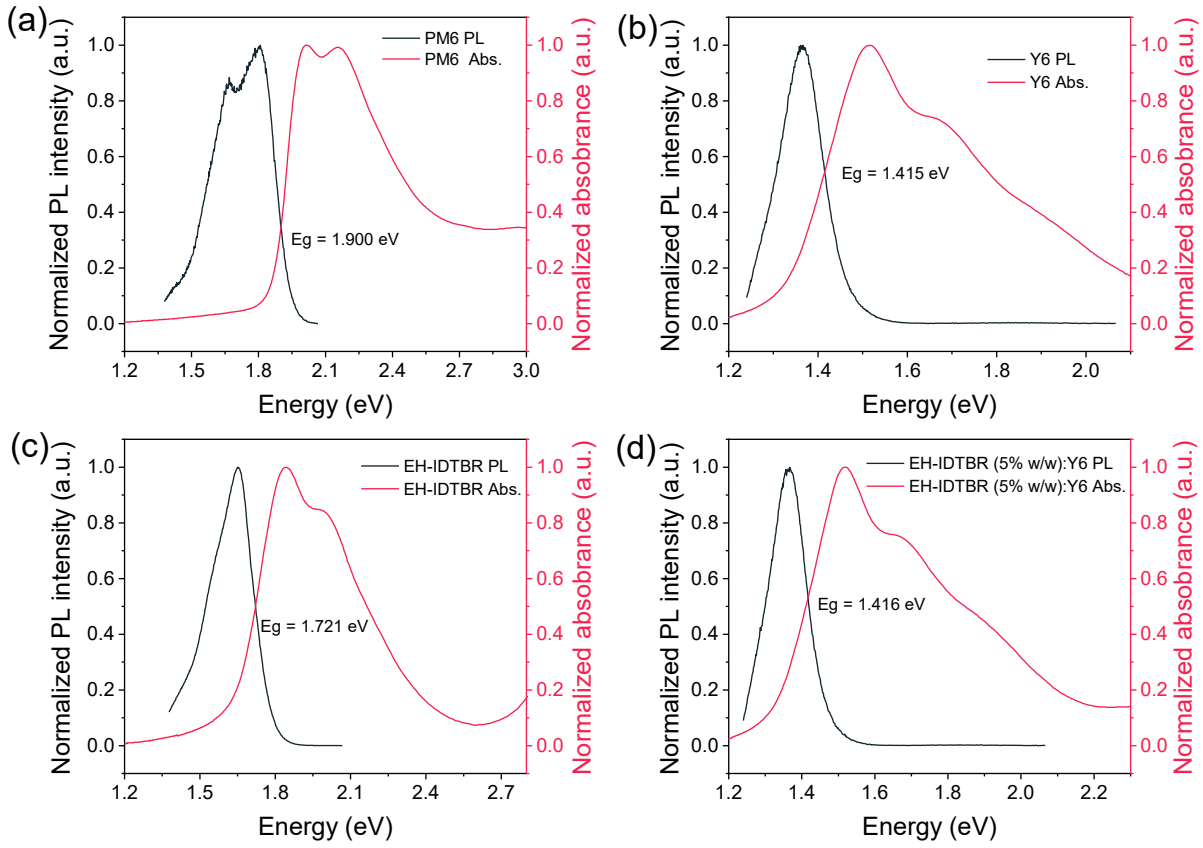

Fig. S24. PL and UV–vis spectra for (a) PM6, (b) Y6, (c) EH-IDTBR and (d) EH-IDTBR (5% w/w):Y6 films.

ciency > 16.5% based on two compatible nonfullerene acceptors. Adv Mater, 2019, 31, 1905645

[24] Zhan L, Li S, Lau T K, et al. Over 17% efficiency ternary organic solar cells enabled by two non-fullerene acceptors working in an alloy-like model. Energy Environ Sci, 2020, 13, 635

[25] Li K, Wu Y, Tang Y, et al. Ternary blended fullerene-free polymer solar cells with 16.5% efficiency enabled with a higher-LUMO-level acceptor to improve film morphology. Adv Energy Mater, 2019, 9, 1901728

[26] Su D, Pan M A, Liu Z, et al. A trialkylsilylthienyl chain-substituted small-molecule acceptor with higher LUMO level and reduced band gap for over 16% efficiency fullerene-free ternary solar cells. Chem Mater, 2019, 31, 8908

[27] Ma R, Liu T, Luo Z, et al. Adding a third component with reduced miscibility and higher lumo level enables efficient ternary organic solar cells. ACS Energy Lett, 2020, 5, 2711

[28] An Q, Wang J, Gao W, et al. Alloy-like ternary polymer solar cells with over 17.2% efficiency. Sci Bull, 2020, 65, 538

[29] Dong S, Zhang K, Jia T, et al. Suppressing the excessive aggregation of nonfullerene acceptor in blade-coated active layer by using n-type polymer additive to achieve large-area printed organic solar cells with efficiency over 15%. EcoMat, 2019, 1, 12006

[30] Pan M A, Lau T K, Tang Y, et al. 16.7%-efficiency ternary blended organic photovoltaic cells with pcbm as the acceptor additive to increase the open-circuit voltage and phase purity. J Mater Chem A, 2019, 7, 20713

[31] Liu T, Ma R, Luo Z, et al. Concurrent improvement in Jsc and Voc in high-efficiency ternary organic solar cells enabled by a red-absorbing small-molecule acceptor with a high lumo level. Energy En-

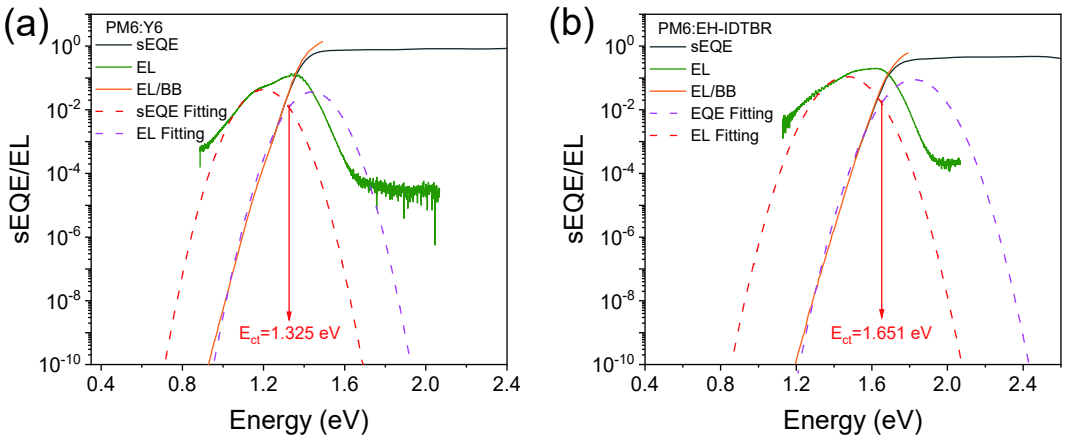

Fig. S25. sEQE and EL spectra for (a) PM6:Y6 and (b) PM6:EH-IDTBR cells.

Table S1. Photovoltaic parameters of PM6:Y6-based ternary OSCs.

The third components	V_{oc} (V)	J_{sc} (mA/cm^2)	FF (%)	PCE (%)	Ref.
PhI-Se:PM6:Y6	0.845	25.7	75.5	16.4	[17]
PM6:BTR:Y6	0.839	25.8	76.7	16.6	[18]
PM6:DRTB-T-C4:Y6	0.85	24.79	81.3	17.13	[19]
PM6:J71:Y6	0.85	25.55	76	16.5	[20]
PM6:PDHP-Th:Y6	0.85	26.6	71.7	16.8	[21]
PM6:Y6:C8-DTC	0.873	26.5	75.61	17.52	[22]
PM6:Y6:3TP3T-4F	0.85	25.9	74.9	16.7	[23]
PM6:Y6:BTP-M	0.875	26.56	73.46	17.03	[24]
PM6:Y6:IDIC	0.868	25.39	74.92	16.51	[25]
PM6:IY6:IN-4F	0.85	25.7	74.5	16.3	[26]
PM6:Y6:ITCPTC	0.861	25.674	78.8	17.42	[27]
PM6:Y6:MF1	0.853	25.68	78.61	17.22	[28]
PM6:Y6:N2200	0.83	26.3	76	16.6	[29]
PM6:Y6:$PC_{71}BM$	0.861	25.1	77.2	16.7	[30]
PM6:Y6:SY3	0.855	25.51	78.2	17.07	[31]
M6:SM1:Y6	0.831	25.7	77.5	16.55	[32]
PM6:Y6:$PC_{61}BM$	0.845	25.4	77	16.5	[33]
PM6:Y6:O-IDTBR	0.85	25.75	76	16.6	[34]
PM6:PM7:Y6	0.848	26.17	76.7	17.02	[35]
PM6:S3:Y6	0.856	25.86	79.17	17.53	[36]
PM6:EH-IDTBR:Y6	**0.853**	**26.03**	**79.22**	**17.59**	This work

viron Sci, 2020, 13, 2115
[32] Yan T, Ge J, Lei T, et al. 16.55% efficiency ternary organic solar cells enabled by incorporating a small molecular donor. J Mater Chem A, 2019, 7, 25894
[33] Yu R, Yao H, Cui Y, et al. Improved charge transport and reduced nonradiative energy loss enable over 16% efficiency in ternary polymer solar cells. Adv Mater, 2019, 31, 1902302
[34] Gasparini N, Paleti S H K, Bertrandie J, et al. Exploiting ternary blends for improved photostability in high-efficiency organic solar cells. ACS Energy Lett, 2020, 5, 1371
[35] Zhang M, Zhu L, Zhou G, et al. Single-layered organic photovoltaics with double cascading charge transport pathways: 18% efficiencies. Nat Commun, 2021, 12, 1
[36] An Q, Wang J, Ma X, et al. Two compatible polymer donors contribute synergistically for ternary organic solar cells with 17.53% efficiency. Energy Environ Sci, 2020, 13, 5039

Table S2. Photovoltaic parameters of the cells with different EH-IDTBR contents.

EH-IDTBR in acceptors (w/w)	V_{oc} (V)	J_{sc} (mA/cm^2)	$J_{Int.}$ (mA/cm^2)	FF (%)	PCE (%)
0%	0.836	25.78	24.48	77.15	16.63
5%	0.853	26.03	24.81	79.22	17.59
10%	0.855	26.00	25.01	77.41	17.06
20%	0.867	25.82	24.60	75.54	16.91
30%	0.872	25.46	24.34	73.45	16.30
50%	0.878	23.72	22.71	61.19	12.74
80%	0.954	7.34	6.98	31.56	2.21
100%	1.18	9.92	9.47	57.75	6.75

Table S3. Parameters from the J_{ph}–V_{eff} plots.

Active layer	J_{sat} (mA/cm^2)	J_{sc} (mA/cm^2)	J_{max} (mA/cm^2)	J_{sc}^*/J_{sat} (%)	$J_{max}^{\&}/J_{sat}$ (%)
PM6:Y6	26.60	25.78	23.76	96.92	89.32
PM6:EH-IDTBR:Y6	26.82	26.03	24.42	97.05	91.05
PM6:EH-IDTBR	11.17	9.92	7.18	84.79	64.28

J_{sat}: The J_{ph} under condition of V_{eff} = 3 V.
J_{sc}^*: The J_{ph} under short-circuit conditions.
$J_{max}^{\&}$: The J_{ph} under maximum power output conditions.

Table S4. Electron and hole mobilities of the blend films with different EH-IDTBR contents.

EH-IDTBR in acceptors (w/w%)	μ_e (10^{-4} cm^2/(V·s))	μ_h (10^{-4} cm^2/(V·s))	μ_e/μ_h
0%	4.31	3.74	1.15
5%	4.54	4.43	1.03
10%	4.86	4.37	1.11
20%	4.08	3.59	1.14
30%	3.77	3.32	1.14
50%	1.16	2.70	0.43
80%	0.63	2.75	0.23
100%	4.22	2.95	1.43

Table S5. GIWAXS parameters.

	Lamellae				π–π stacking			
Blends	q (Å^{-1})[a]	d-spacing (Å)	FWHM (Å^{-1})[c]	CCL (Å)[c]	q (Å^{-1})[a]	d-spacing (Å)	FWHM (Å^{-1})[b]	CCL (Å)[c]
PM6:Y6	0.296	21.22	0.094	60.13	1.767	3.554	0.275	20.55
PM6:EH-IDTBR:Y6	0.296	21.22	0.072	78.50	1.774	3.540	0.258	21.91
PM6:EH-IDTBR	0.30	20.93	0.057	99.16	1.750	3.589	0.419	13.49

[a] Scattering peak position;[b] Half-width at diffraction peak;[c] Crystal coherence length.

Table S6. The parameters used to calculate energy loss.

Blend	J_{sc} (A/m^2)	E_{CT} (eV)	λ (eV)	f (eV)	V_{rad} (meV)
PM6:Y6	257.8	1.325	0.1192	0.0101	231
PM6:EH-IDTBR:Y6	260.3	1.334	0.1197	0.0144	240
PM6:EH-IDTBR	99.2	1.651	0.1782	0.0382	295

Table S7. Energy loss details.

BHJ blends	E_g^* (eV)	E_{CT} (eV)	V_{oc} (V)	$E_g - eV_{oc}$ (eV)	$E_g - E_{CT}$ (eV)	$E_{CT} - eV_{oc}$ (eV)	ΔE_{rad} (eV)	$\Delta E_{non\text{-}rad}$ (eV)
PM6:Y6	1.415	1.325	0.836	0.579	0.09	0.489	0.231	0.250
PM6:EH-IDTBR:Y6	1.416	1.334	0.853	0.563	0.082	0.481	0.240	0.233
PM6:EH-IDTBR	1.721	1.651	1.18	0.541	0.07	0.471	0.295	0.168

*E_g of the blend films were estimated from the intersection point of absorption and emission spectra.